AGU100 ADVANCING EARTH AND SPACE SCIENCE

JGR

Journal of Geophysical Research: Atmospheres

RESEARCH ARTICLE

10.1029/2018JD029438

Key Points:

- First simultaneous temperature comparisons from collocated Rayleigh and Na lidars were made over one annual cycle
- Good agreement was found in the two lidars' temperatures from 85 to 95 km
- Significant temperature differences were found above 95 km and below 85 km

Correspondence to:
L. Sox,
leda.sox@gtri.gatech.edu

Citation:
Sox, L., Wickwar, V. B., Yuan, T., & Criddle, N. R. (2018). Simultaneous Rayleigh-scatter and sodium resonance lidar temperature comparisons in the mesosphere-lower thermosphere. *Journal of Geophysical Research: Atmospheres*, *123*. https://doi.org/10.1029/2018JD029438

Received 13 JUL 2017
Accepted 20 AUG 2018
Accepted article online 30 AUG 2018

Author Contributions

Conceptualization: Leda Sox, Vincent B. Wickwar, Tao Yuan, Neal R. Criddle
Data curation: Leda Sox, Tao Yuan
Formal analysis: Leda Sox, Tao Yuan
Funding acquisition: Leda Sox, Vincent B. Wickwar, Tao Yuan
Investigation: Leda Sox, Vincent B. Wickwar, Tao Yuan, Neal R. Criddle
Methodology: Leda Sox, Vincent B. Wickwar, Tao Yuan, Neal R. Criddle
Supervision: Vincent B. Wickwar
Validation: Leda Sox
Visualization: Leda Sox
Writing - original draft: Leda Sox
Writing – review & editing: Leda Sox, Vincent B. Wickwar, Tao Yuan, Neal R. Criddle

Simultaneous Rayleigh-Scatter and Sodium Resonance Lidar Temperature Comparisons in the Mesosphere-Lower Thermosphere

Leda Sox[1,2], Vincent B. Wickwar[2], Tao Yuan[2], and Neal R. Criddle[2]

[1]Electro-Optical Systems Laboratory, Georgia Tech Research Institute, Atlanta, GA, USA, [2]Center for Atmospheric and Space Sciences and Physics Department, Utah State University, Logan, UT, USA

Abstract The Utah State University (USU) campus (41.7°N, 111.8°W) hosts a unique upper atmospheric observatory that houses both a high-power, large-aperture Rayleigh lidar and a Na lidar. For the first time, we will present 19 nights of coordinated temperature measurements from the two lidars, overlapping in the 80–110 km observational range, over one annual cycle (summer 2014 to summer 2015). This overlap has been achieved through upgrades to the existing USU Rayleigh lidar that increased its observational altitude from 45–95 to 70–115 km and by relocating the Colorado State Na lidar to the USU campus. Previous climatological comparisons between Rayleigh and Na lidar temperatures have suggested that significant temperature differences exist between the two techniques. This new comparison aims to further these previous studies by using simultaneous, common-volume observations. The present comparison showed the best agreement between 85 and 95 km, with a temperature difference, averaged over the whole data set, of about 1.1 ± 0.5 K. Larger differences occurred above and below these altitudes with the Rayleigh temperatures being colder by about 3.5 ± 0.5 K at 82 km and warmer by up to 9.1 ± 3.5 K above 95 km.

1. Introduction

The mesosphere-lower thermosphere (MLT) region of the Earth's upper atmosphere is host to many important atmospheric features and phenomena which warrant both short- and long-term measurements of densities, temperatures, and winds. Observations of these parameters have been conducted over the past several decades with various instruments, including in situ techniques from sounding rockets and remote sensing techniques from satellites, ground-based airglow instruments, and lidars.

Lidar techniques remain the most advantageous and robust method for acquiring temperature measurements in terms of both vertical and temporal resolution. The two most widely used lidar techniques in the MLT are Rayleigh-scatter lidar and sodium (Na) resonance lidar. Rayleigh lidar systems measure elastic backscatter from neutral N_2, O_2, Ar, and O particles in the atmosphere. Rayleigh lidar backscatter measurements give relative density profiles, which are then used to calculate absolute temperature profiles (Hauchecorne & Chanin, 1980; Sox, 2016). Na lidar measures resonant fluorescence scattering from sodium atoms that form a layer in the 80–105 km region where meteoric ablation occurs. With proper design, Na lidars can measure the thermal broadening and Doppler shift of the laser-induced Na resonance fluorescence spectrum. From this, Na density, temperature, and winds can be deduced (Fricke & von Zahn, 1985; Krueger et al., 2015; She et al., 1992).

Long-term observations of the middle atmosphere and MLT at several lidar sites have resulted in climatological and trend studies of the temperature structure in this region (Argall & Sica, 2007; Beig et al., 2003; Funatsu et al., 2011; Hauchecorne et al., 1991; Herron, 2007; Leblanc et al., 1998; She et al., 2000, She, Krueger, et al., 2015; States & Gardner, 2000; Wynn, 2010; Yuan et al., 2008). The Rayleigh and Na lidar facilities used in these studies each underwent a great deal of testing through model simulations (Rayleigh) or analyses of atomic physics (Na), which gave researchers high confidence in the two techniques. However, the two techniques have yet to be compared with one another using many simultaneous, collocated observations. Two of these studies compared climatological results from the two lidar techniques based on measurements at different geographic locations (Argall & Sica, 2007; Leblanc et al., 1998). The first study used data sets from Rayleigh lidars located at the Observatoire d'Haute-Provence (43.6°N, 5.4°E) and Centre d'Essais des Landes (44.3°N, 1.2°W) and the Na lidar at Colorado State University (CSU; 41°N, 105°W; Leblanc et al., 1998). The second study compared data sets from the large aperture Rayleigh lidar at the Purple Crow

Table 1
Approximate Signal and Background Levels for the Utah State University Rayleigh Lidar

Date	1-year average (10^6 counts per second)	1-year average (photon counts per 2 min)
Signal (at 70 km)	0.640	575
Background noise + dark count (averaged from 189 to 339 km)	0.022	20
Dark count[a] (no light on tube)	0.006–0.022	6–20

[a]Dark count was measured independently during testing and was different for each of the three Electron Tubes 9954 photomultiplier tubes used for the 2014–2015 observations.

Lidar (PCL; 42.5°N, 81.2°W) in Canada with the aforementioned Observatoire d'Haute-Provence and Centre d'Essais des Landes lidars in France and with those from the Na lidars at both CSU and Urbana, Illinois (40°N, 88°W; Argall & Sica, 2007). A third set of measurements gave a comparison between temperatures from the PCL Rayleigh lidar and a collocated Na lidar for a few nights (Argall et al., 2000). Both climatological studies showed good agreement between Rayleigh data sets at similar latitudes, but all three papers showed significant differences between the Rayleigh and sodium data sets.

The Rayleigh lidar system located on the campus of Utah State University (USU; 41.7°N, 111.8°W) has recently undergone a series of major upgrades in order to increase its observational range from 45–95 to 70–115 km. These upgrades included employing two Nd:YAG lasers, operating at 532 nm, to achieve greater transmitted power and increasing the receiving area of the system's telescopes from 0.15 to 4.9 m^2. This resulted in an increase in the power-aperture product (PAP), or lidar system figure-of-merit, from 2.7 to 206 W/m^2. By extending the USU Rayleigh lidar's altitude range farther into the MLT region, significant overlap with the typical observational range of Na lidar systems (~80–105 km) has been achieved. The only other Rayleigh system with a comparable PAP is the PCL Rayleigh system, though they reported slightly less overlap with the Na lidar range (Argall & Sica, 2007).

In summer 2010, the Na lidar system, developed and operated at CSU since 1990, was relocated to the same site on the USU campus as the Rayleigh lidar system. By summer 2014, both lidar systems were independently making regular observations with occasional concurrent nocturnal observations. This work focuses on 19 such simultaneous observations made by the two lidar systems between summer 2014 and summer 2015. To the best of our knowledge, this is the first study with a significant number of simultaneous, collocated Rayleigh and Na lidar measurements, covering the full 80–110 km altitude range.

The remainder of this paper is organized as follows: in section 2 technical descriptions of both the Rayleigh and Na lidar systems at USU are given, as well as explanations of their respective data sets and data analysis methods; in section 3 the temperature results from the two systems are compared in several ways; and finally, in sections 4 and 5, respectively, a discussion and conclusions from this comparison are presented.

2. Description of USU Rayleigh and Na Lidars

2.1. USU Rayleigh Lidar System and Data Analysis Description

The large-aperture, high-power, Rayleigh lidar began operating at the Atmospheric Lidar Observatory on the campus of USU during the summer of 2014 (Sox, 2016; Wickwar et al., 2016). It employs two Spectra Physics GCR series Nd:YAG lasers that are frequency-doubled to operate at a wavelength of 532 nm and, at this same wavelength, transmit a total output power of 42 W (1,400 mJ per pulse) with a pulse repetition rate of 30 Hz (the two lasers' pulses being offset by 62 ns). The telescope receiver is composed of four parabolic primary mirrors, each 1.25 m in diameter and each focusing directly onto the end of an optical fiber. The cone of light is contained within the numerical aperture of the fiber. The light from the four fibers is then combined optically and sent to an Electron Tubes 9954 series photomultiplier tube (PMT). The low-altitude signal and background are reduced by a mechanical chopper and a 1-nm FWHM interference filter placed in front of the PMT. For all of the nights reported in this study, the highest count rates (at the lowest altitude, ~70 km) did not exceed a 1 MHz count rate, well within the linear range of the PMT. Average count rates of the signal at 70 km, average background or noise level (see next paragraph), and dark count are given in Table 1 for the full June 2014 to June 2015 Rayleigh data campaigns. A more detailed list of the Rayleigh lidar's system parameters is given in Table 3.

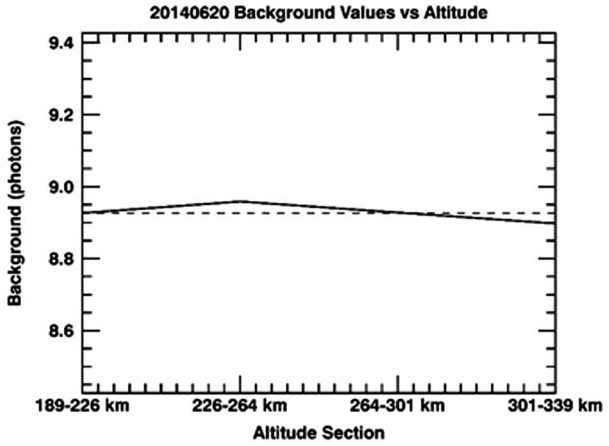

Figure 1. Background values averaged over the whole night of 20 June 2014 and at four different altitude intervals (189–226, 226–264 km, etc.). The average background value for the full 189 to 339 km altitude range is given by the dashed line.

The raw signal is binned in 250-ns, or 37.5-m, intervals using a multichannel scaler unit, with a time resolution of 2 min and then recorded to a PC. In postprocessing, the data are averaged over either 1-hr periods or the part of the whole-night observing period common to both lidar systems. The chopper is set to be open for a long altitude range in order to get a good average value for a given night's background, or noise, level. Background values are calculated for each 2-min profile by averaging in altitude from 189 to 339 km (over 4,000 altitude bins); then from these values, an average background for the whole night is calculated (more detail in Sox, 2016, similar methods used in McCullough, 2015). The background values are averaged over such a large altitude range in order to get a very good estimate for the night's average background value. The Rayleigh lidar temperature retrieval is quite sensitive to background subtraction. If the average background value is overestimated, the derived temperatures will become warmer at the highest altitudes and the opposite is true if the background is underestimated. In building the detector system and in operating procedures, special attention was paid to keep background values constant with altitude. Indeed, we have found the background levels to be quite stable across the whole 189 to 339 km altitude range, which gives confidence in our average background value calculations (see Figure 1 for an example of how the background stays steady with altitude).

The time-averaged, background-subtracted signal at altitude h is then represented by $\overline{S}_h$ and given by

$$\overline{S}_h = \overline{S+N}_h - \overline{N}, \tag{1}$$

where $\overline{N}$ is the measured background averaged over both time and altitude and $\overline{S+N}_h$ is the measured signal plus background at altitude h averaged in time and smoothed in altitude about altitude h. The brackets represent time averages and the averaging bar represents averages or smoothing in altitude. The smoothing of the signal plus background is by a Hanning filter with a 2-km FWHM window. The average background and the background-subtracted signal at the top altitude are given for each night in Table 2. The standard deviation of the background-subtracted signal, at altitude h, over j time bins, and vertically smoothed with a 2-km FWHM Hanning filter centered on $i = 0$ is

$$\sigma_{\overline{S}_h} = \sqrt{\frac{1}{jf_{107}^2}\left\{\Sigma_{i=-53}^{53} F_i^2 S + N_j\right\} + \frac{1}{jk}\overline{N}_{kj}}, \tag{2}$$

where the average background value $\overline{N}$ was averaged over j time bins and k altitude bins and F_i/f_{107} is the normalized Hanning coefficient calculated at each point, i. For this study, $k = 4{,}000$ altitude bins and j is equal to the number of 2-min integrations recorded for the whole night, which varied from 126 to 354. These large values of k and j kept $\sigma_{\overline{S}_h}$ very small (see Table 2). A perhaps surprising result is that the average, background-subtracted signal at the maximum altitude is a small fraction of the averaged background (Table 2). This comes about because of the large number of background samples and the large number of signal samples and plays a large role in our criteria for choosing a maximum altitude as described below.

For each night's average, the Rayleigh lidar's upper altitude limit was chosen to be where the background-subtracted signal was 20 times the standard deviation given in equation (2). Several factors determined how good the signal-to-standard deviation ratio was at a given altitude for each observed night, including length of the observation, laser power, how many lasers were used (a maximum of two: GCR 6's maximum power is 24 W, GCR 5's maximum power is 18 W), how many mirrors were used (a maximum of four, each approximately 1.25 m in diameter), atmospheric transmission, neutral number density, and phase of the moon. Depending mostly on the number of hours in each night's average and how many lasers and mirrors were used (or the PAP, see Table 2 for a listing of these values for each night), the upper altitude limit varied from 100 to 110 km, but reached 105 km, on average.

Table 2
Estimated Rayleigh PAP, Average Background, and Measured Signal

Date	Laser power (W)	Area (m^2)	PAP (W/m^2)	$\overline{N}^a$ (photons)	$\overline{S}^a$ at h_{max} (photons)	$\sigma_{\overline{S}}$ at h_{max} (photons)	h_{max} (km)	# of hours
140620	42	4.91	206	8.93	0.65	0.033	113	4.2
140702	42	4.91	206	8.52	0.54	0.027	113	5.9
140717	18	4.91	88.4	18.7	0.76	0.038	105	6.5
140722	18	4.91	88.4	8.58	0.53	0.027	106	6.1
140723	18	4.91	88.4	7.76	0.50	0.025	108	6.3
140724	18	4.91	88.4	10.1	0.58	0.029	105	6.0
140912	18	3.68	66.3	25.7	0.94	0.047	104	5.7
140913	18	3.68	66.3	18.8	0.63	0.032	101	9.2
140925	18	3.68	66.3	5.37	0.34	0.017	109	9.3
140926	18	4.91	88.4	6.50	0.41	0.021	109	7.8
141029	24	4.91	118	19.9	0.76	0.038	107	6.7
141104	24	4.91	118	36.7	1.08	0.054	107	6.1
141106	42	4.91	206	93.9	1.94	0.097	106	4.8
141108	42	4.91	206	61.3	1.00	0.050	109	11.8
141109	42	4.91	206	65.2	1.04	0.053	107	11.4
150328	42	4.91	206	4.90	0.36	0.018	103	7.7
150414	42	4.91	206	3.42	0.39	0.020	103	4.7
150610	24	4.91	118	3.16	0.38	0.019	101	4.6
150618	24	4.91	118	3.59	0.36	0.18	103	5.6

Note. PAP = power-aperture product.
[a]Photons per altitude bin (37.5 m) and time bin (2 min).

The whole-night averaged Rayleigh lidar signal profiles were then used to calculate absolute temperatures using a modified version (Beissner, 1997; Herron, 2004) of the method described in Hauchecorne and Chanin (1980). This method uses the proportionality between lidar signal and relative atmospheric density to calculate absolute temperatures using the ideal gas law and the assumption that the measured part of the atmosphere is in hydrostatic equilibrium. This results in an integral equation that is calculated going down in altitude and requires an initial condition, or a seed temperature, at the highest altitude. The effect of the seed temperature decreases exponentially as the integral steps down in altitude (Beissner, 1997; Herron, 2004, 2007; Leblanc & McDermid, 1998; Sox, 2016). For this study, the seed temperature was taken from the Na lidar temperature profile for 18 out of the 19 nights. On 25 September 2014, when the Rayleigh lidar temperatures started at a higher altitude than the Na lidar temperatures, the seed temperature was taken from the Naval Research Lab's Mass Spectrometer Incoherent Scatter (NRLMSISE-00) empirical model (Picone et al., 2002) at 6 UT for the corresponding date. The standard deviation in the calculated temperatures is then found through error propagation and is given at an altitude h by

$$\sigma_{T_h} = \sqrt{T_h^2\left(\frac{\sigma_{n_h}}{n_h}\right)^2 + \left[\sigma_{T_{hmax}}^2 + T_{h_{max}}^2\left(\frac{\sigma_{n_{h_{max}}}}{n_{h_{max}}}\right)^2\right]e^{\frac{-2(h_{max}-h)}{H}}} \tag{3}$$

(Gardner, 1989), where subscript h is the altitude of interest and h_{max} is the upper altitude for a given night (found using equation (2)), T is the temperature, n is the relative number density, σ_n is the uncertainty in the relative number density, and H is the atmospheric scale height, which is assumed to be a constant 7 km in our calculations. The number density n is proportional to the background subtracted signal S, which can be seen in a simplified version of the elastic lidar equation given by

$$S(h) = C\frac{n(h)}{h^2}, \tag{4}$$

where n is the number density, $1/h^2$ is the range-squared correction, and C is a constant that combines several values that are assumed constant over small changes in altitude including atmospheric transmission, backscatter coefficient, receiver solid angle, and so on. The ratio of σ_{n_h}/n_h in equation (3) is thus

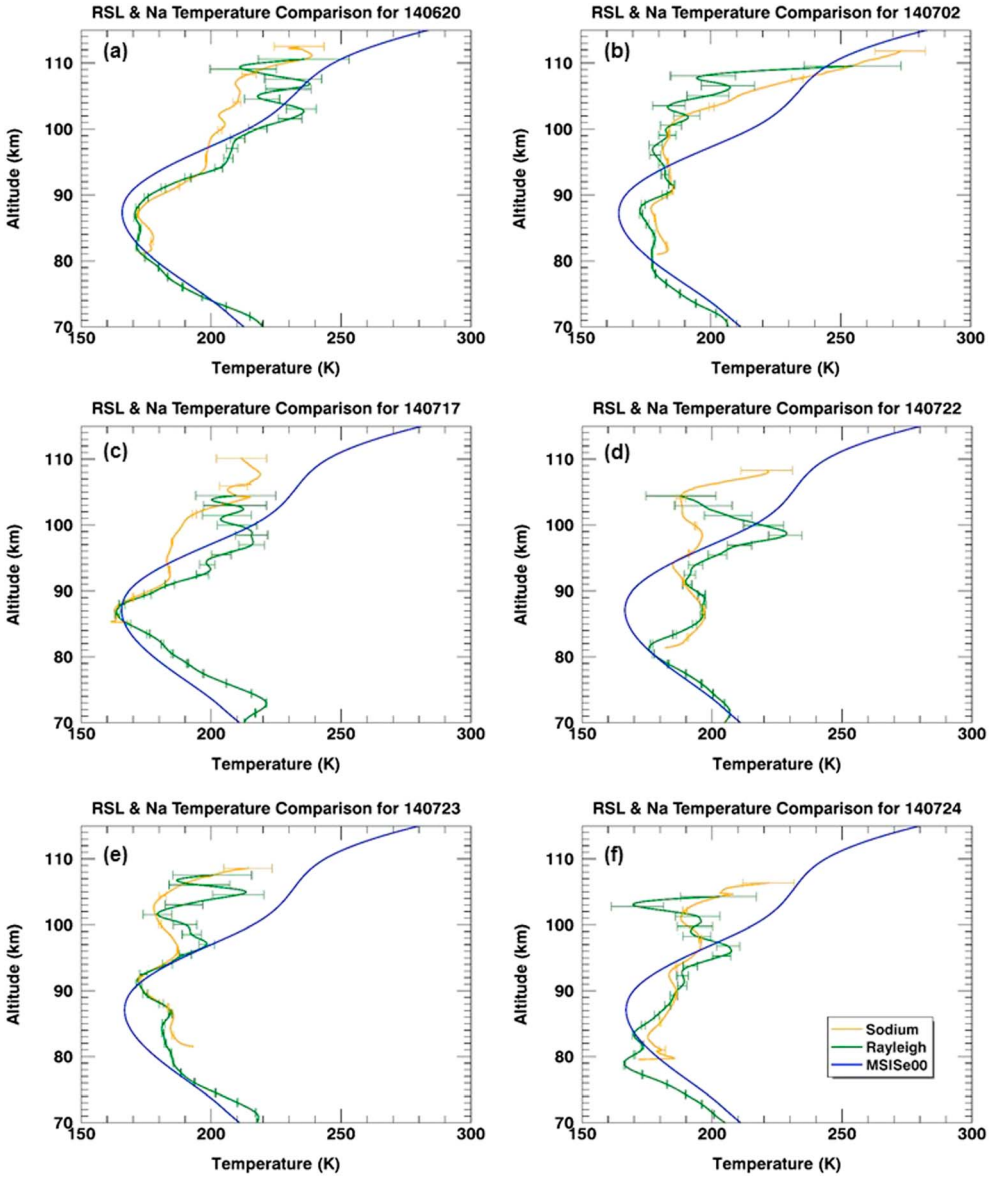

Figure 2. Summer 2014 temperature-altitude plots for whole-night averages measured using the Rayleigh lidar (green curves) and Na lidar (orange curves). Naval Research Lab's MSIS model temperatures (blue curves) are also given for each date at 6 UT. RSL = Rayleigh-scatter lidar; MSIS = Mass Spectrometer Incoherent Scatter.

equal to the ratio of the uncertainty in the background subtracted signal (given by equation (2)) to the whole-night averaged, altitude-smoothed background subtracted signal (given in equation (1)). For this study we used Na lidar temperatures as Rayleigh lidar seed temperatures and thus have used the Na temperature uncertainty values for the second term in equation (3). For the night of 25 September 2014 when a NRLMSISE-00 value was used as the Rayleigh seed temperature the same value of $\sigma^2_{T_{hmax}}$ was taken from the Na uncertainty values for the following night (26 September 2014). It should be noted that for the Rayleigh technique, the temperature errors are the largest (~15 K for the 19 nights of this study) at the top of the profile and exponentially decrease to less than a 1 K within about 15 km from the top altitude. Close examination of the Rayleigh curves in Figures 2–5 show this behavior. Average values of the Rayleigh temperature errors over these 19 nights are also given in Table 3, which show about 15 K at the highest altitude error bars, about 1 K at a midrange altitude (~93 km), and 0.1 K at the lowest altitude (70 km).

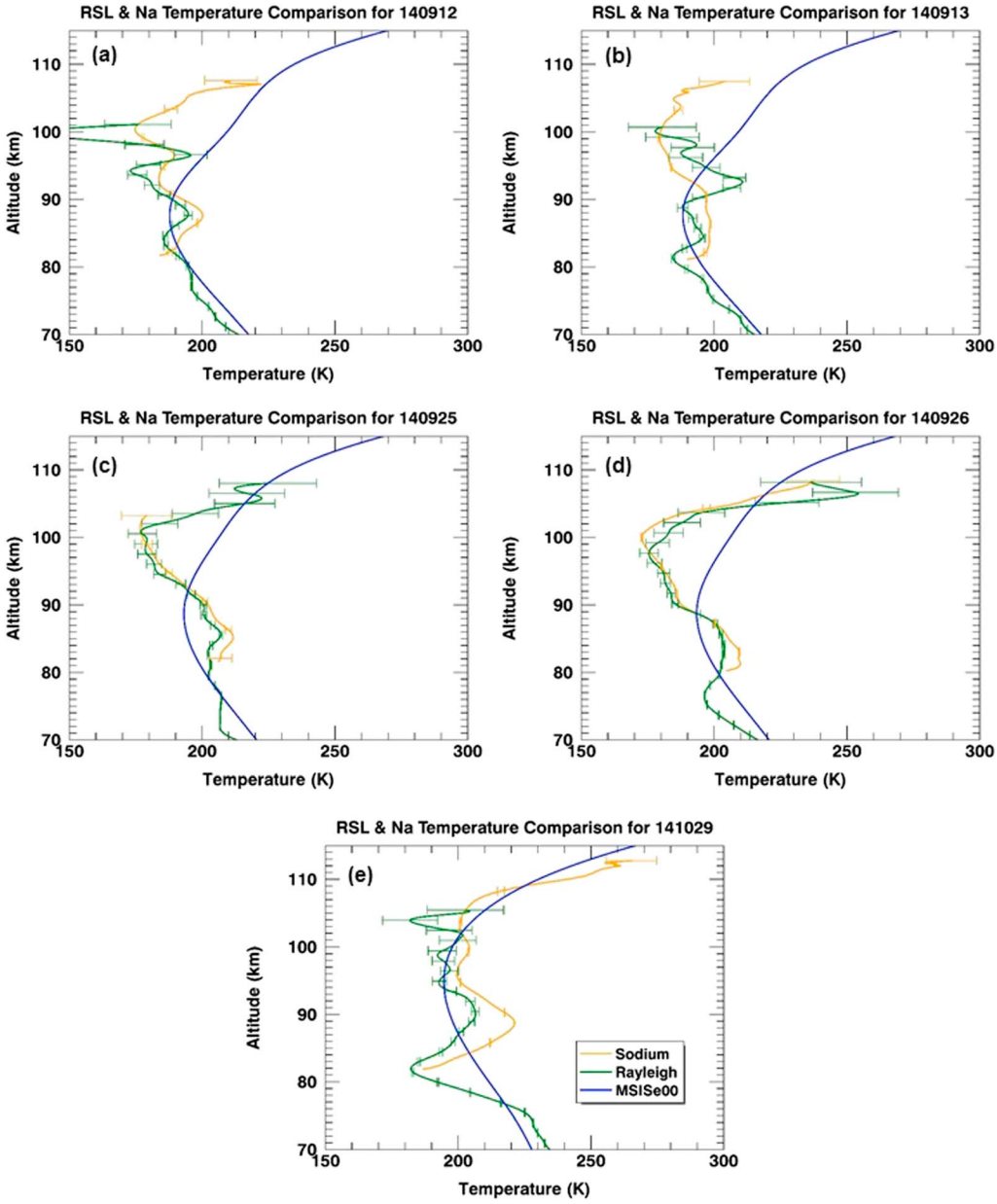

Figure 3. Same as Figure 2 but for the fall 2014 portion of the overlapping data set. RSL = Rayleigh-scatter lidar; MSIS = Mass Spectrometer Incoherent Scatter.

2.2. USU Na Lidar System and Data Analysis Description

The configuration of the Na lidar and subsequent data analysis used to acquire the neutral temperatures presented in this paper are explained in detail by Krueger et al. (2015). In short, the USU Na lidar employs a continuous-wave (CW) ring, dye laser, frequency locked to the Na D_{2a} line. The CW laser beam is then sent through a dual, acousto-optic modulator that enables the laser's frequency to be shifted up and down relative to the Na D_{2a} line to produce three frequencies (D_{2a} + 630 MHz, D_{2a}, D_{2a} − 630 MHz). Each of these three frequencies' CW laser beam is converted into laser pulses using a pulsed dye amplifier pumped by a single-mode, Nd:YAG laser with a 50 Hz repetition rate. The small frequency shift that occurs during this laser-pulse amplification process is measured by a subsystem that utilizes iodine absorption spectroscopy and is corrected in the lidar data analysis (Yuan et al.,

2009). This Na Doppler lidar utilizes the Master Oscillator Power Amplifier technique to produce narrow bandwidth laser pulses (~120 MHz FWHM) at the Na D_2 line. The seed laser for this Master Oscillator Power Amplifier system is the aforementioned CW ring, dye laser (Coherent 899), outputting ~300 mW, which is well above the laser dye saturation level of the laser amplifier. Thus, the resulting bandwidth of all the lidar's laser pulses have the same saturation bandwidth. This bandwidth is measured regularly by the Na lidar group. In addition, the Na lidar splits its total laser power of ~1.0 W into two or three directions. With a laser beam divergence angle of ~0.8 mrad, the energy of these laser pulses are well below the Na atom saturation level. Based on the information provided by Hamamatsu Corporation for the Na lidar PMT (H7421-40), the saturation rate is 1.5 million counts per second for 30 ns pulses for every PMT sampling, which is corresponding to per bin per shot in the lidar measurement. The USU Na lidar has been using a modified version of the H7421-40 since 2008, which generates ~9 ns pulses, and the saturation level becomes ~ 4.5 million counts per second. This can be converted to 4,500 counts per bin for every 1,000 laser shots, setting the upper limit of the PMT saturation for the lidar measurement. The maximum signal level of the USU Na lidar so far is around 1,500 per bin for 1,000 laser shots near the peak of the mesospheric Na layer (~91 km during early winter), well below the PMT saturation level. Therefore, the PMTs in the USU Na lidar system are performing linearly. Since the transmitted beam is split into a three-beam pointing configuration, it necessitates having three telescope receivers and detectors, one for each returned signal. Each of these is used to determine line-of-sight Doppler-shifted spectra from which winds, Na densities, and temperatures are derived.

The collision frequency between Na atoms and neutral molecules is great enough that the Na and neutral temperatures are assumed to be the same (Krueger et al., 2015). With the insertion of a Faraday filter (Chen et al., 1996), the Na lidar is also able to make daytime observations. However, in this study only the nighttime data were used in order to overlap with the Rayleigh lidar's measurements. The Na lidar return signals were recorded with a 1 μs, or 150 m, bin size and a 1-min time resolution. A Hanning window with a 2 km FWHM was utilized to smooth the lidar data in the vertical direction. The data were averaged in time over both 1-hr periods and the part of the whole-night observing period common to both lidar systems. For the Na lidar, the whole-night mean temperatures were calculated by averaging the 1-hr temperatures together. Average Na temperature error values are given for high-altitude, midaltitude, and low-altitude ranges in Table 3. Our cutoff for plotting at the high end of the Na lidar's measurement range was where the temperature errors were equal to 10 K. Near the bottom edge of the Na layer, we cutoff where the temperature errors were equal to 10 K and the temperature gradient dT/dz changed rapidly with altitude.

The three-frequency technique allows the Na lidar to detect Doppler shifts and Doppler broadening of the mesospheric Na atoms' resonance spectrum simultaneously. The Na lidar temperature reduction uses the relationship between the three frequencies of the returned signal and the detailed theoretically calculated shape of the Na spectrum to relate the lidar signal to atmospheric temperatures, winds, and Na densities (Krueger et al., 2015; She, Chen, et al., 2015).

Parameters from both the Rayleigh and Na lidar systems are given in Table 3. In the MLT, the Na density ($10^9/m^3$) is many orders of magnitude (~9) smaller than the neutral (N_2, O_2, and Ar) density. However, the cross section per steradian, for Na at 589 nm, is some 17 orders of magnitude greater than the cross section for Rayleigh scatter at 532 nm (Kent & Wright, 1970; Measures, 1992). The net effect is that Na resonance scattering is about eight orders of magnitude more efficient than Rayleigh scattering in the altitude range of the mesospheric Na layer. For this reason, the Na lidar is able to obtain good signal levels in the MLT region using much less transmitted power and smaller receiving-aperture area than the Rayleigh lidar. However, the Na lidar's overall measurement range is limited by the altitude distribution of the mesospheric Na layer, which is on average located between 80 and 105 km (e.g., Yuan et al., 2012). Some sporadic Na events have been observed at lower geomagnetic latitudes reaching up to 140 and 170 km (Gao et al., 2015; Liu et al., 2016), however. The Rayleigh lidar's measurement range, in contrast, is limited by advances in instrumentation (laser power, telescope size, and detector sensitivity). It needs to achieve an appropriate level of signal-to-standard deviation, which decreases exponentially with altitude as the neutral density in the atmosphere decreases and by range-squared from the laser.

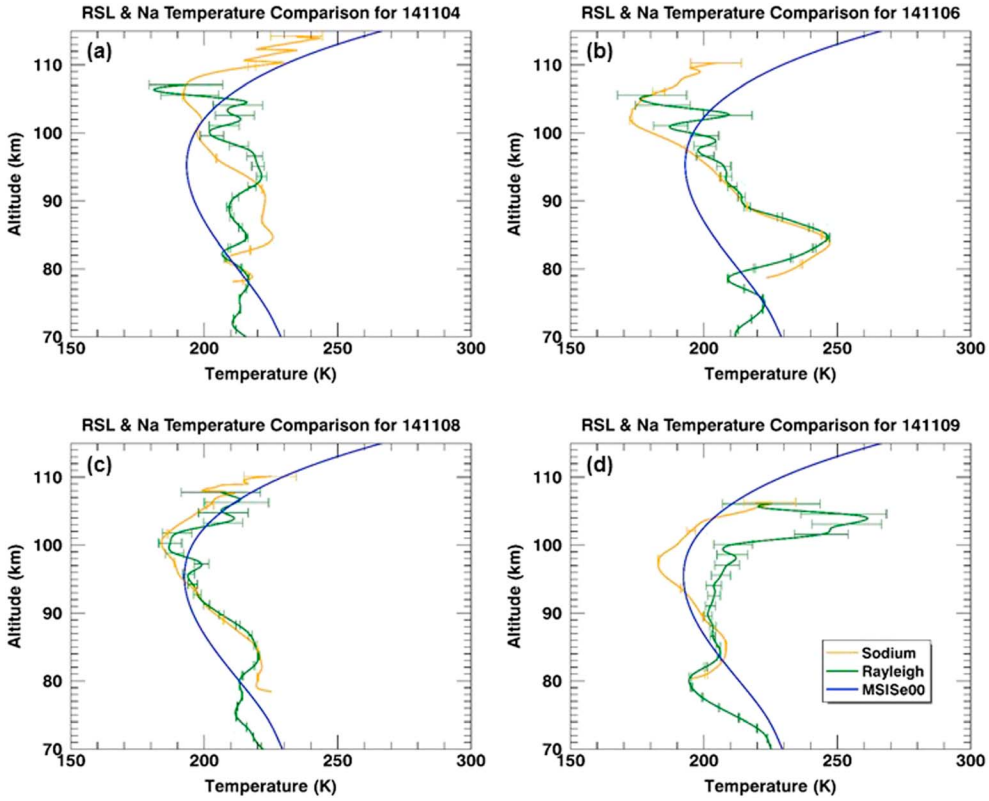

Figure 4. Same as Figure 2 but for the winter 2014 portion of the overlapping data set. RSL = Rayleigh-scatter lidar; MSIS = Mass Spectrometer Incoherent Scatter.

3. Observations and Results

Between summer 2014 and summer 2015, there was a total of 19 nights (see Table 4) when the two lidars made simultaneous measurements for at least 4 hr during the night. The overlap between the two lidars' sets of observations is relatively small due to the different observational schedules that were employed by each group. The Na lidar group conducts observations over full, clear diurnal cycles, and typically runs its campaign once a month for 3–5 days and nights. Since the Rayleigh lidar cannot currently operate in the daytime, the Rayleigh group aims to observe over as many clear nights as possible throughout the year.

3.1. Whole-Night Average Temperature Comparison

Whole-night averages of temperature were calculated for each lidar's data set. The averages are at least 4 hours long, and the beginning and end times for each lidar were selected to be within 2 min of one another. Temperature profiles from each lidar, along with a profile from the NRLMSISE-00 model, are in Figures 2–5 for the 19 nights. Each set of plots represents a different seasonal period. The error bars were calculated by propagating the measurement error (from photon counting) through the smoothing and each lidar's respective temperature reduction process.

Often, the best agreement between the two sets of lidar temperatures is found between about 85 and 95 km in altitude (Figures 2–5). Above 95 km, there are significant differences between the two sets of temperatures on many nights (see Figures 2a-2d, 3a-3b, 4a-4b, 4d, 5a, and 5c) and typically result in Rayleigh lidar temperatures being warmer than Na lidar temperatures. The largest temperature differences, of up to 30–80 K, occur at higher altitudes (above 100 km). However, because the seed temperature for the Rayleigh reduction (section 2.1) is the Na temperature on most of these nights, there is a likely bias that reduces the temperature difference. On a few nights, the Rayleigh temperatures show wave-like oscillations and the Na temperatures do not (Figures 2a, 2e, and 4b). However, these oscillations occur in the high-altitude regions where the Rayleigh temperature uncertainties are the highest, so we do not suspect that they are significant. Below

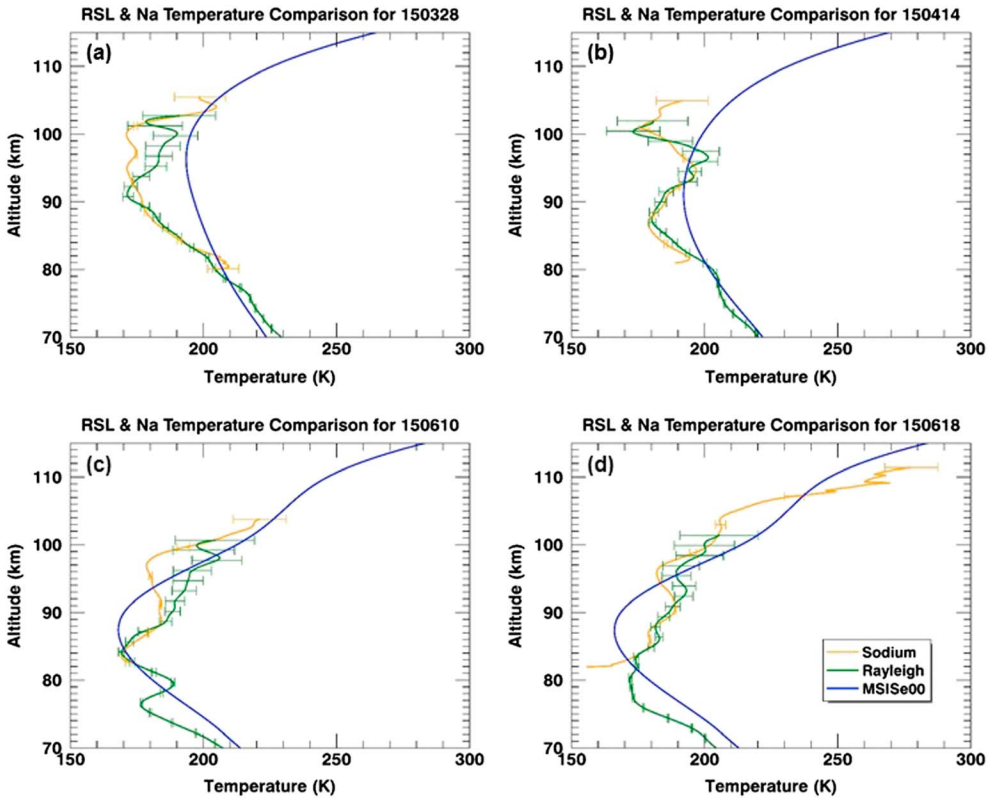

Figure 5. Same as Figure 2 but for the spring and summer 2015 portions of the overlapping data set. RSL = Rayleigh-scatter lidar; MSIS = Mass Spectrometer Incoherent Scatter.

85 km, the Na lidar temperatures are typically warmer than the Rayleigh temperatures (Figures 2a–2b, 2d–2f, 3, 4b–4d, and 5a). The magnitude of the temperature differences in this region is smaller than that at higher altitudes, but still found to be statistically significant on most nights (e.g., Figures 6a–6b, see section 3.2).

The two lidars' temperatures agree much better with one another than they do with the NRLMSISE-00 model temperatures. For the most part, if one lidar's temperature profile is either warmer or colder than the NRLMSISE-00 temperatures, then the other lidar's temperature profile behaves in the same way. There are a few exceptions though, as in Figures 2a, 2c–2d, 4d, and 5c. In most of these cases, above 90 km, the Na

Table 3
Comparison of Whole-Night Averaged Rayleigh and Sodium Lidar System Parameters

System parameter	Rayleigh lidar	Na lidar
Emitted laser wavelength (nm)	532	589 ± υ
Laser energy (mJ per pulse)	1,400	20–30 (per transmitted υ)
Total transmitted laser power (W)	42	~1 (per transmitted υ)
Laser repetition rate (Hz)	30	50
Transmitted beam divergence (mrad)	0.125	0.8
Receiving aperture (m^2)	4.86 (4 mirrors)	0.45 (1 mirror)
Vertical resolution after smoothing (km)	2	2
Maximal altitude range (km)	70–110	78–114
Estimated error at top[a] (K)	15.0	9.7
Estimated error at midrange (~93 km; K)	1.0	0.3
Estimated error at bottom[b] (K)	0.1	9.7

[a]Top altitudes for Rayleigh lidar, h_{max}, vary and are described in section 2.1; top altitudes for Na lidar taken to be where uncertainty was equal to 10 K. [b]Bottom altitude for Rayleigh lidar set to 70 km; bottom altitudes for Na lidar taken to be where uncertainty was equal to 10 K and dT/dz changed rapidly with altitude.

Table 4
Dates for 2014–2015 Temperature Data Set

Index number	Date (YYMMDD)	Index number	Date (YYMMDD)
0	140620	17	141029
1	140702	18	141104
2	140717	19	141106
3	140722	20	141108
4	140723	21	141109
5	140724	36	150328
10	140912	37	150414
11	140913	41	150610
12	140925	42	150618
13	140926		

temperatures are colder than NRLMSISE-00 temperatures whereas Rayleigh temperatures are warmer. While the structure of the lidars' temperature profiles are roughly similar to the NRLMSISE-00 structure, there are a few cases where the observed lidars' mesopauses (temperature profile minima) are at different altitudes than the NRLMSISE-00 mesopause (Figures 2d–2f, 3, 4a–4c, and 5).

The temperature difference could have a seasonal dependence and a dependence on lidar technique (Na temperatures warmer at lower altitudes and Rayleigh temperatures warmer at higher altitudes). In subsection 3.2 we will investigate the possible seasonal dependence and in subsections 3.3. and 3.4 will explore some differences in the two techniques.

3.2. Seasonal Temperature Comparison

To better compare the two lidar data sets seasonally, the temperatures from each lidar at six specific altitudes are plotted in a time series in the upper panels of Figure 6. Differences between the two lidars' temperatures are shown in the lower panels of Figure 6. In Figures 6a and 6f, the lack of either lidar's data points indicates when temperatures were not available at those specific altitudes. Error bars are also plotted for the uncertainty in each lidar's individual temperature values and for the uncertainty in the temperature differences (lower panels). Also, note that the vertical axis for the difference plot at 105 km (Figure 6f) has a different scale than the other five plots. Though the overlapping lidar data set covers one annual cycle, the data coverage over winter 2014–2015 is sparse. In order to show gaps in the data but still keep the plots visually legible, an indexing system was applied to the actual calendar dates when the lidar observations were made. The dates and their respective indices are given in Table 4.

The time series plots show that at and below 90 km, the Rayleigh temperatures are generally colder than the Na temperatures (on average about 2.7 ± 0.4 K colder). At 95 km and above, the Rayleigh temperatures are generally warmer than the Na temperatures (on average about 6.5 ± 3.0 K warmer). Between 85 and 95 km, the temperature differences are at their lowest (on average 0.4 ± 0.5 K). This agrees with the behavior seen in the largest temperature differences in Figures 2–5. The lower panels of Figure 6 show that at all altitudes, there does not appear to be a strong seasonal dependence in the difference between the two temperature data sets. Rather, there is a dependence on altitude with the most agreement (smallest differences) occurring between 85 and 95 km and the least agreement (largest differences) below 85 km and above 95 km. The average difference values at different altitudes are given in Table 5.

3.3. Temperature Perturbation Comparison

Hourly temperature perturbations were calculated from both lidars' temperature measurements for four nights and shown in Figure 7. These four nights were chosen to give examples of wave-like activity in the different seasons. To calculate the perturbations, each lidar's whole-night average was subtracted from each lidar's respective hourly averages. Data from the east Na lidar beam were used and all of the hourly Rayleigh temperatures were seeded with values from the Na hourly temperature profiles. The two lidars' hourly temperature perturbations display very similar structure. The lidars capture approximately the same wave parameters, which were estimated visually from the plots and are given in Table 6 for the four selected nights. While there are differences in absolute temperature between the two lidars' measurements, the fact that the temperature perturbations measured by each lidar are almost identical show that the two different lidar techniques are capable of capturing the same atmospheric dynamics. Also, the two lidars, even though pointing in slightly different directions, are not measuring different portions of the same wave-like structure.

3.4. Preliminary Temperature Difference Investigation

3.4.1. Comparison of Lidar Beam Pointing Directions

One possible explanation for the temperature differences between the two techniques is that the beam-pointing directions are different. The Rayleigh lidar transmits solely in the zenith whereas the Na lidar typically operates with a three-beam pointing configuration: one beam pointing to the east (20° off-zenith), one to the west (20° off-zenith), and one to the north (30° off-zenith). This configuration enables the determination of horizontal wind and zonal momentum flux (Acott et al., 2011). All the data shown in the previous

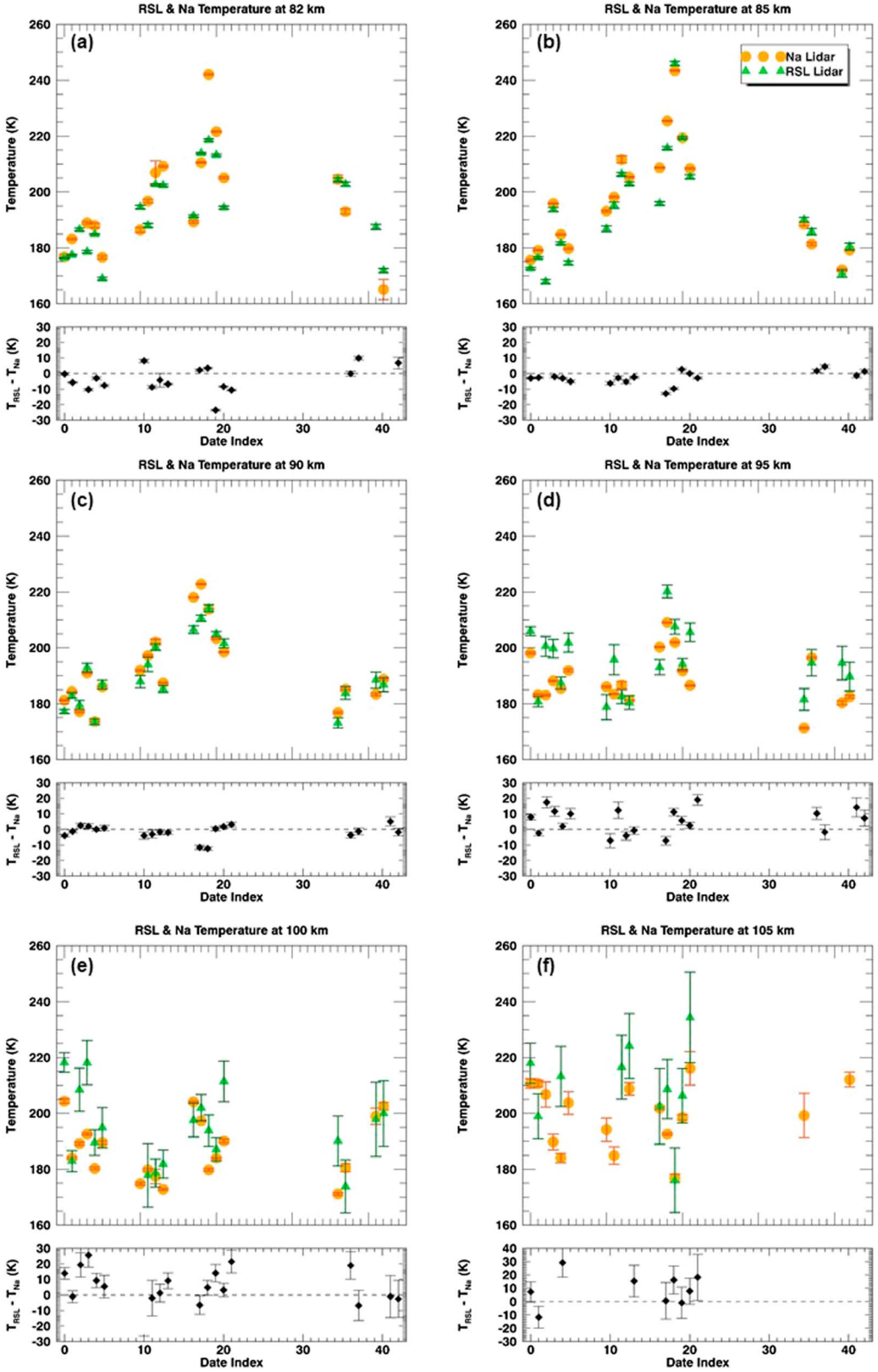

Figure 6. Rayleigh and Na lidar temperature time series at 82 (a), 85 (b), 90 (c), 95 (d), 100 (e), and 105 km (f) along with the differences between the two lidars' temperatures (lower panels, black diamonds). Note the scale change in (f) for the temperature differences. The relationship between date index and calendar date is given in Table 4. RSL = Rayleigh-scatter lidar.

Table 5
Average Differences Between Rayleigh and Na Lidar Temperatures at Specific Altitudes

Altitude (km)	$\overline{T_{Raylegh} - T_{Na}}$ (K)	$\sigma_{\overline{T_{Raylegh} - T_{Na}}}$ (K)
82	−3.5	0.5
85	−2.8	0.2
90	−1.7	0.4
95	5.6	0.8
100	4.8	1.8
105	9.1	3.5

section were acquired using the east-pointing Na lidar beam. At higher altitudes (~110 km), this separates the east-pointing Na lidar beam and Rayleigh lidar beam by about 40 km in the horizontal east–west direction. In the MLT region, persistent, large amplitude (~20 K) large gravity waves have been observed at the USU location (Herron et al., 2007; Yuan et al., 2014), which, if they existed on these nights, might account for the differences seen in the two temperature data sets when one of these waves covered only one lidar beam for several hours. Thus, by including the west pointing beam from the Na lidar (~73 km away from the east beam at an altitude of 100 km), we can see if such a wave existed on those nights with large temperature differences.

The west-pointing beam data from the Na lidar were only available on 11 of the 19 overlapping nights due to a different campaign configuration. Figure 8 shows four temperature profile plots with curves for Rayleigh temperature and the east- and west-beam Na temperatures. These four nights were chosen to show two nights when the Rayleigh and Na temperatures had large differences (Figures 8a and 8c), a

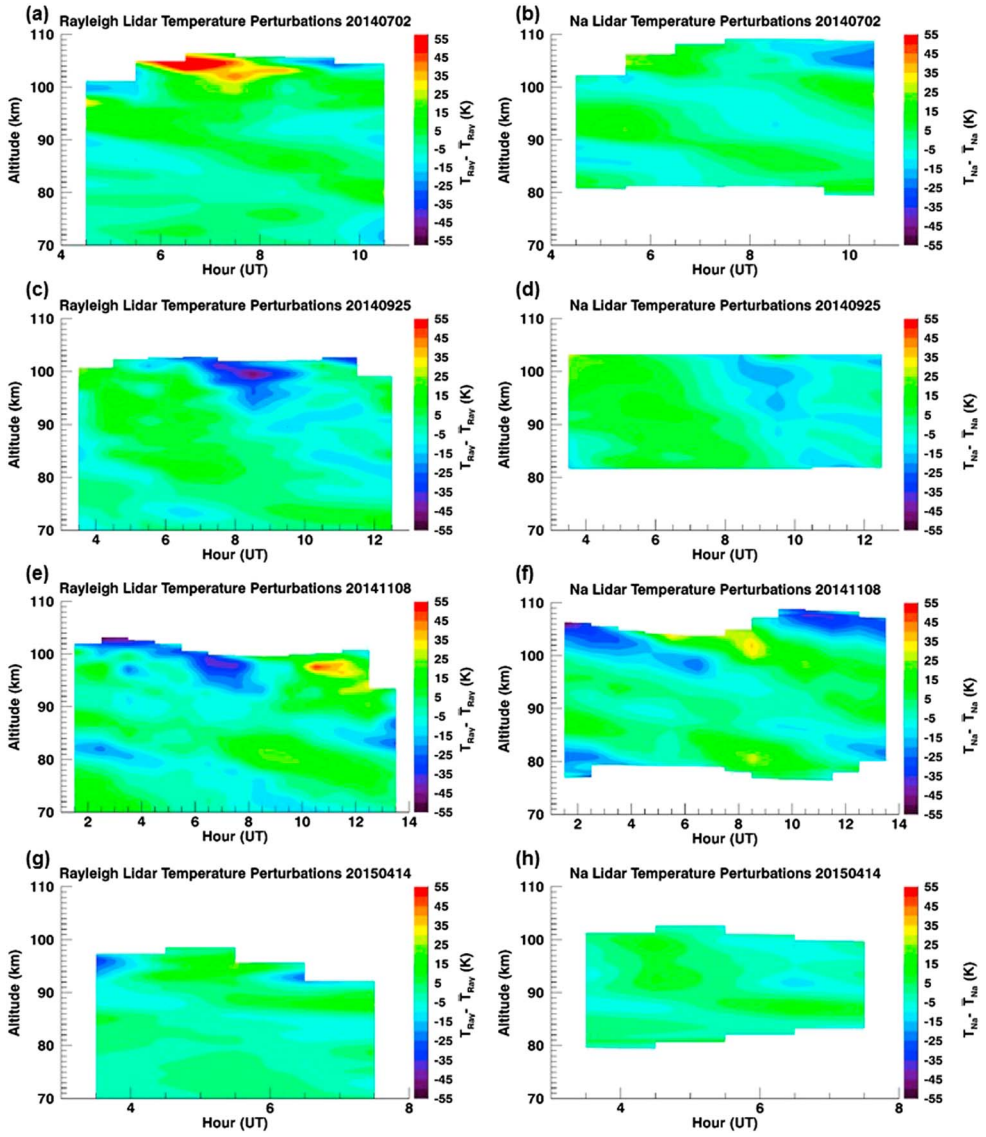

Figure 7. Temperature perturbations (night mean subtracted from hourly means) from Rayleigh lidar data (left panels) and Na lidar data (right panels).

Table 6
Approximate Wave Parameters Obtained From Hourly Temperature Perturbations

	Rayleigh lidar		Na lidar	
Date (YYMMDD)	Period (hour)	Phase velocity (km/hr)	Period (hour)	Phase velocity (km/hr)
140702	6.8	−2.4	8.0	−2.4
140925	8.3	−3.4	NA	−3.3
141108	13.1	−1.8	11.7	−1.5
150414	7.4	−2.2	NA	−2.0

night when the two sets of temperatures agreed well (Figure 8b), and a night when the east- and west-beam temperatures disagreed the most (Figure 8d). Error bars have been removed to make the plots more visually legible, but the west-beam temperature error bars are in the same order of magnitude as the east-beam error bars seen in Figures 2–5. From Figure 8, one notes that the differences between the east- and west-beam Na temperatures do not, in general, account for the differences in temperatures between the Na and Rayleigh lidars. In the two cases where taking the average of the east- and west-beam Na data might give better agreement with Rayleigh temperatures (e.g., from about 100–105 km in Figure 8d), there are still significant differences up to 45 K in the two lidars' temperatures (e.g., near 98 km in Figure 8a and near 104 km in Figure 8c). Figure 8d showed the only case in the 11 nights where the east Na beam agreed better with the Rayleigh temperatures than with the west Na beam, though this was only over about 3 km. From these representative plots, it is clear that the pointing direction of the Na lidar does not greatly affect the temperature profiles and thus does not explain the large differences between the Na and Rayleigh profiles, implicating such temperature differences are not due to large scale long period gravity waves. It is still possible that there was a wave propagating mostly in the meridional direction and confined between the two Na lidar beams, passing only the Rayleigh beam. However, this horizontal scale would categorize such a wave as a small-scale wave with high frequency, which should not appear in nightly averaged temperature profiles.

3.4.2. Influence of Atomic Oxygen

It is known that at altitudes above about 90 km, the proportion of atomic oxygen O increases gradually with altitude (Chapman, 1930; Wulf & Deming, 1938). The effect of changing composition on the Rayleigh backscatter cross section (RBCS) and mean molecular mass (MMM) might affect the Rayleigh temperature calculations, which usually assume constant RBCS and MMM throughout the measurement region. However, the effects of changing RBCS and MMM on the Rayleigh lidar temperature data reduction have been studied using both models (Argall, 2007) and measurements (Sox, 2016). Figure 9 shows four temperature-difference curves calculated using Rayleigh temperature data from 22 July 2014. The black curve is the difference between temperature determined for changing MMM and RBCS (using the method described in Sox, 2016) and the temperatures that assume constant composition (shown in Figure 2d). Accounting for the presence of O in NRLMSISE-00, and thus changing the MMM and mean RBCS, is found to reduce the Rayleigh lidar temperatures by less than 2 K in the 85–115 km region. While one might expect the temperature difference to increase with altitude as the proportion of O increases, the top-most temperature is unchanged because it is determined by the seed temperature. Such small temperature differences are negligible compared to the much larger differences seen between the Na and Rayleigh temperatures in Figure 2d and thus do not explain the differences between the two lidar techniques' measurements. The blue, green, and red curves in Figure 9 are an attempt to determine the amount by which the proportion of O has to be increased to bring the Rayleigh and Na temperatures into much better agreement. The proportion of O is increased by 100% (blue curve), 900% (green curve), and 1,900% (red curve; i.e., 20 times the original amount given by NRLMSISE-00), and MMM and RBCS are changed accordingly. The changes in corrected and uncorrected Rayleigh temperature are the largest above 90 km, which is also the location of the largest Rayleigh and Na temperature differences. The final increase of 1,900% to the NRLMSISE-00 O values above 90 km gave a change in the magnitude of the Rayleigh temperatures that is comparable to the magnitude of the difference between the two lidars' temperatures on this night. However, the change in temperature above 90 km is in the opposite direction (warmer, not colder) to account for the difference between the two lidars' temperatures. Since adding more O appears to make Rayleigh temperatures warmer, we do not think our Rayleigh temperature reduction is underestimating the amount of O present in this region. It should be noted, however, that simply adding a large amount of O, as in Figure 9, violates the hydrostatic equilibrium condition of the Rayleigh temperature retrieval (Hauchecorne & Chanin, 1980). With this in mind, collaborations with modelers could help improve this O correction method.

It should be also noted that the Sox (2016) composition-correction method is restricted by the limited number of measurements of atomic oxygen that exist and are inputs for the NRLMSISE-00 model. More can be

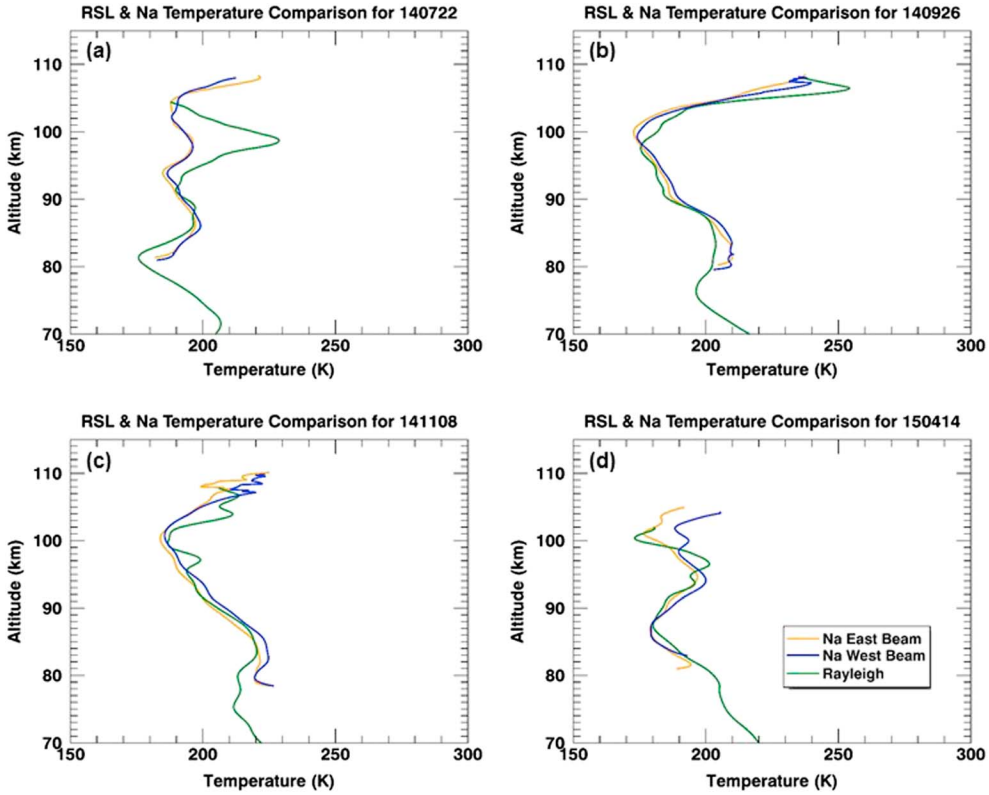

Figure 8. Temperature profile plots similar to those in Figures 2–5. The Rayleigh lidar profiles are in green, the east-pointing Na lidar profiles are in orange, and the west pointing Na lidar profiles are in blue. It is often hard to distinguish among the east, west, and average Na profiles because they are superposed over much of the altitude range. RSL = Rayleigh-scatter lidar.

done to improve this method by experimenting with more observations made with different instruments and different model formulations. If, in fact, changing MMM was found to be the main cause for the differences between the two lidars' temperatures, then a method such as that described in Mwangi et al. (2001) could be used to deduce number-density profiles of N_2, O_2, and O in the 80–110 km region.

3.4.3. The Effects of Changing PAP, Background Subtraction, Na Layer Edges, and Temperature Uncertainty

Possible variations in both lidars' observations related to changing instrumentation and data analysis should be discussed in terms of possible effects on the two lidars' temperature differences.

First, it was mentioned earlier in this paper that the number of lasers and mirrors the Rayleigh lidar used, and thus its PAP, changed from night-to-night. Estimates of the PAP for each night are given in Table 2. By comparing the changes in PAP to the differences seen between the two lidars in Figures 2–5, one can see that changes in PAP do not occur at the same time as changes in the magnitude of the temperature difference. For example, 12 September 2014 (Figure 3a) has a relatively low PAP and 20 June 2014 (Figure 2a) has a high PAP; however, the maximum differences between the two lidars' temperatures above 95 km are both approximately 30 K. Table 2 also lists the average background value and background-subtracted signal from the Rayleigh lidar for each night. One can see that some nights (e.g., all of the November 2014 nights) have higher signal than others. Again, comparing the changes in signal level to the differences in the two lidars' temperatures night-to-night does not show any relationship (e.g., compare Figures 2a, 3a, and 4d and the corresponding signal levels given for these dates in Table 2).

Figures 2a, 2c, 2d, and 4d indicate that the two lidar temperatures differ mostly in the altitude range above ~92 km, the top half of the main mesospheric Na layer. Figures 3b and 4a reveal that, sometimes near the centroid height of the main Na layer, the two temperatures differ. This shows that, even though the Na density is high enough to generate reliable Na lidar temperature, such a temperature difference sometimes exists. Therefore, we conclude that these temperature differences are not related to insufficient Na echo

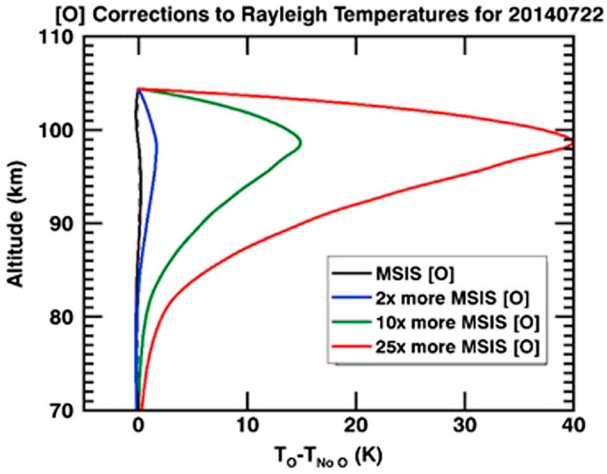

Figure 9. Temperature difference curves showing the difference between Rayleigh temperatures modified for the presence of O using NRLMSISE-00 values and those that have not been modified (black curve). The difference between modified temperatures, which have 25 times the amount of O that NRLMSISE-00 gives, and unmodified temperatures is shown in red, those that have 10 times the NRLMSISE-00 amount are in green, and those that have 2 times the NRLMSISE-00 amount are in blue. NRLMSISE-00 = Naval Research Lab's Mass Spectrometer Incoherent Scatter.

levels. The nightly averaged Na density profiles on 20 June and 12 September 2014, when some of the largest temperature differences were observed, are shown in the Figure 10 on a log scale. The Na layer that night can be seen to extend well into the lower thermosphere with Na density of 10s of atoms per cubic centimeters near 105 km.

Finally, the statistical significance of the temperature differences between the two lidars should be explored. Temperature uncertainties are plotted for each lidar's temperatures in Figures 2–6. At both high altitudes (above 95 km) and low altitudes (85 km and below) there are many examples of the difference between the two temperatures being larger than either lidar's error bars. Figure 6 shows this the most clearly. At low altitudes (Figures 6a–6c), the error bars for each lidar are quite small so most of the differences between the two are not covered by either lidars' error bars. Higher in altitude (Figures 6d–6f), both lidars' error bars get larger with Rayleigh error bars becoming larger more rapidly. At 105 km, some of the Rayleigh error bars do span the temperature difference, so the differences between the two lidars at very high altitudes could be less than what is shown in Figures 2–5. However, there are still some nights (20 June 2014, 02 July 2014, 23 July 2014, 12 September 2014, and 26 September 2014) when the temperature differences are statistically significant. Table 5 gives values for the average temperature differences at the five altitudes shown in Figure 6. The best agreement appears between 85 and 95 km, with an average temperature difference of about 1.1 ± 0.5 K (the average of these three values in Table 5). Larger differences exist above and below these altitudes with the Rayleigh temperatures being colder by about 3.5 ± 0.5 K at 82 km, and warmer by up to 9.1 ± 3.5 K above 95 km.

4. Discussion

On the same nights at USU, the Rayleigh lidar temperatures are shown to be colder than those of the Na lidar between 80 and 90 km (Figures 6a–6c and many curves in Figures 2–5; averages of these values are given in Table 5). A similar observational conclusion was made by Argall and Sica (2007) using climatological data from different sites. Without simultaneous measurements, they compared Rayleigh and Na lidar climatologies from several different sites at roughly the same latitude, but they were several hundred kilometers apart in longitude over an overlapping altitude range of about 80–95 km. They found that on average, the Rayleigh temperatures were 7 K cooler. Our data show the Rayleigh temperatures being colder from 82 to 90 km by 2.7 ± 0.4 K on average and then warmer by 5.6 ± 0.8 K at 95 km. Leblanc et al. (1998) showed an earlier comparison of Rayleigh and Na lidar climatologies from sites that, again, were not collocated. The overlapping altitude region for the Rayleigh and Na lidars in Leblanc et al. (1998) was shifted downward, compared to Argall and Sica (2007). Nonetheless, Leblanc et al. (1998) again showed that the Rayleigh temperatures were colder than the Na temperatures in the 80–88 km region (their Figure 1). From 82 to 88 km, the Rayleigh temperatures were 2–6 K colder than the Na temperatures, which is close to what we observe. Between 80 and 82 km, Leblanc et al. (1998) show that the difference between the two lidars' temperatures becomes even greater with the Rayleigh temperatures being between 8 and 14 K colder than the Na temperatures. At 82 km, our Rayleigh temperatures are on average 3.5 ± 0.5 K colder than our Na temperatures, which is a smaller difference but in the same direction as the Leblanc et al. (1998) results.

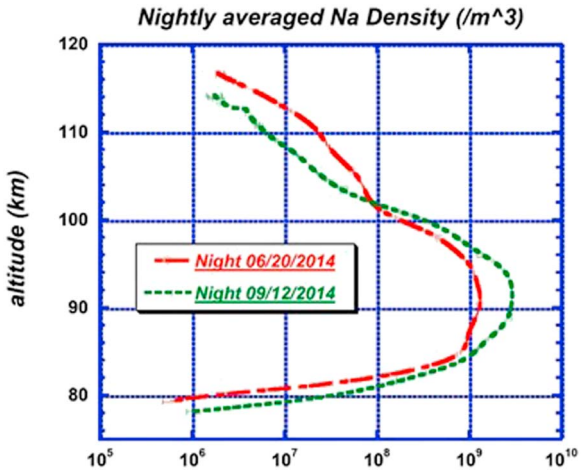

Figure 10. Nightly average Na density for the nights of 20 June 2014 (red) and 12 September 2014 (green).

At altitudes (95–105 km) higher than the upper limits of both studies' climatologies, our data show that the Rayleigh temperatures are on

average increasingly warmer with increasing altitude, reaching an average maximum temperature difference of about 9.1 ± 3.5 K at 105 km (Figures 6d–6f, Table 5) with an average of 6.5 ± 2.3 K over the entire 95–105 km range. These unique results cannot be compared with the previous climatological studies because their overlapping measurements did not extend into these high altitudes. The simultaneous comparison plots in Argall et al. (2000) did extend from 80 to 100 km; however, the three plots did not show a conclusive pattern in temperature difference between the two techniques. It can be noted that the differences between the two sets of temperatures in the Argall et al. (2000) measurements did reach maximum magnitudes of ~15 K, which is similar to the maximum magnitudes found in the present study (Table 5).

Leblanc et al. (1998) suggested that the differences in Rayleigh and Na lidar climatologies could be explained by their choice of taking the Rayleigh initialization information (either temperature or pressure) from the CIRA-86 model (Fleming et al., 1990). In Argall and Sica (2007), this idea was dispelled by using the CSU Na temperatures as initialization values for the PCL Rayleigh lidar temperature reduction. Their results still showed large differences between the two lidars' climatologies. Our results similarly show significant temperature differences with either Na lidar or NRLMSISE-00 initialization values.

From there, Argall and Sica (2007) went on to suggest that the difference in the two climatologies could be caused by the geographical separation of the Rayleigh and Na lidar sites. They argued that the distance between the lidar sites could allow for changes in planetary or gravity wave activity which could explain the differences they saw between the Rayleigh and Na climatologies. By eliminating the geographical separation of the lidar sites, our study shows that this is unlikely to be the cause of the differences between the two techniques' temperatures. Additionally, as described earlier, the east- and west-pointing Na beams, which are 80 km apart at that altitude, have practically the same temperatures.

Temperature differences proposed by Argall et al. (2000) and further explored in Mwangi et al. (2001), are caused by changes in atmospheric composition in the measurement region. Mwangi et al. (2001) showed that, assuming this is the primary cause for temperature differences, then the photon counts from the Rayleigh lidar and temperature profile from the Na lidar can be used to solve initial-value problems in order to obtain absolute density profiles of N_2, O_2, and O. We have taken a different approach and do not assume that the differences in temperature are necessarily due to changing atmospheric composition. To test this approach, we used our method of correcting for changing atmospheric composition, given in **s**ection 3.4.3, to show that the effects of changing composition on Rayleigh temperatures do not account for the differences found between the two lidars' temperatures. This method does rely heavily on the NRLMSISE-00 model, however, and so the Rayleigh temperature reduction could potentially be improved with a source of N_2, O_2, and O density measurements.

Thus, we have shown that simultaneous and collocated Rayleigh temperatures are colder than Na temperatures below 85 km. This is in agreement with two other comparisons, which were based on climatological temperatures from different locations. An important question is to find potential mechanisms inducing this well-established difference. Both techniques are based on solid physics principles; the Rayleigh on hydrostatic equilibrium and the ideal gas law, the Na on the shape of the sodium fluorescence spectrum.

Looking at the region below 85 km, the Rayleigh observations are well within their usual altitude range. Being well below the turbopause, the constituents should be well mixed with the same proportions as at lower altitudes. If there is added atomic oxygen, it should be an extremely small proportion, which would have almost negligible effect on the derived temperatures, as shown above. Since the neutral densities are so much greater than the Na densities, that energized Na atoms from chemical reactions should be thermalized immediately. However, the Na observations are in a region of decreasing Na density. Perhaps low Na densities lead to erroneous temperature determinations. This is especially true near 80 km, where the Na density drops sharply near the bottom edge of mesospheric Na layer.

Looking at the region above 95 km, the Rayleigh technique is pushing into relatively new territory. However, it is still low enough that it should be below the turbopause. Nonetheless, there should be a greater proportion of atomic oxygen. Data reduction experiments have been carried out on the effect of atomic oxygen on the scattering cross section and on the MMM. These do not account for the difference in Rayleigh and Na temperatures. Again, the Na density is decreasing, this time with increasing altitude but rather slowly, compared with the bottom side of Na layer (Figure 10). However, if the temperature differences are due to decreasing Na density at the top and bottom of the Na layer, then this does not necessarily explain the

consistent pattern of Rayleigh temperatures being warmer than Na temperatures above 95 km and colder below 85 km.

The bigger temperature differences are at higher altitudes, near where we expect to transition from the mesosphere into the lower thermosphere, where we expect to encounter the turbopause, and where we have compositional changes. Also, the transition from the dominance of eddy diffusivity to molecular diffusivity in this region may change some of the assumptions in the lidar analysis algorithms. Possibly, these differences are signaling that the transitions are occurring at lower altitudes than expected and more variable in time than expected or are introducing new constituents.

5. Conclusions

We have presented the first comparison of simultaneous temperatures acquired by Rayleigh-scatter and Na-resonance lidars collocated in the same observatory on the campus of USU and covering the same altitude range (~80–110 km). This comparison leads to several conclusions:

1. Our simultaneous, collocated Rayleigh and Na lidar measurements have shown a general pattern of having the best agreement between 85 and 95 km ($\overline{\Delta T} = 1.1 \pm 0.5$ K) and larger differences above and below these altitudes with the Rayleigh temperatures being colder at 82 km ($\overline{\Delta T} = -3.5 \pm 0.5$ K) and warmer above 95 km ($\overline{\Delta T} = 9.1 \pm 3.5$ K).
2. These results agree with previous results (Argall & Sica, 2007; Leblanc et al., 1998) in the lower altitude region below about 95 km. Above 95 km, we have shown the new result of Rayleigh temperatures being warmer than Na temperatures.
3. Temperature perturbations were used to show that the two lidar techniques capture the same wave-like activity over the course of a night.

Instrument configurations were brought into question to investigate the observed differences between the two lidar techniques' temperatures. The west- and east-pointing laser beam configurations of the Na lidar gave approximately the same temperature profiles, meaning that the differences between Rayleigh and Na temperatures are essentially independent of the pointing direction of the Na lidar. This confirms that the discrepancies between the two temperature sets do not arise, for instance, from each lidar measuring different portions of the same wave structure. To further confirm this, the hourly temperature perturbations showed that the two lidars measured approximately the same wave parameters. Changes in Rayleigh PAP, signal level, and corrections for changing composition, as well as linearity effects for both lidars, were all explored and shown not to relate to the temperature differences between the two lidars.

While the mechanism causing the differences between the two lidars' temperatures has yet to be determined, a clue that may prove helpful in working toward a solution is that the differences between the two temperatures change sign with altitude. The Rayleigh temperatures tend to be warmer at higher altitudes (at 95 km and above) and colder at lower altitudes (at 90 km and below) than the Na temperatures. This clue could bring into question the current assumptions about the dynamics and chemical processes that both lidar techniques are based on.

Continued observations from the two collocated lidars will shed light on these unanswered questions. Ideally, enough simultaneous data will be collected from the two USU lidars to obtain good coverage throughout all months in order to further explore the day-to-day and seasonal differences between the two techniques' deduced temperatures. Additionally, comparing lidar temperatures with those from other techniques (e.g., satellites, airglow) and model values will be useful in future investigations.

Acknowledgments
The original Rayleigh lidar was initially upgraded to the much more sensitive configuration with funds from NSF, AFOSR, and USU. The system was further upgraded to bring it online with funds provided by the Space Dynamics Laboratory Internal Research and Development program, USU, the USU Physics Department and personal contributions. Engineering support for these latter upgrades was provided by Matthew Emerick, Thomas Amely, and Ryan Martineau. The Rayleigh data presented in this paper were acquired through the dedicated efforts of many student operators including David Barton, David Moser, Bryant Ward, Joe Slansky, Preston Hooser, Rebecca Petrick, Patrick Sharp, Luis Navarro, Jordan Burns, and Warren Schweigert. The Na lidar was supported under NSF AGS grant number 1135882. The Na data presented in this paper were acquired through the dedicated efforts of many student operators including: Neal Criddle, Xuguang Cai, Brittany Marriott, and Eric Lyman. The authors would also like to thank the anonymous reviewers for their helpful feedback. The Na lidar data from this study are available at the CRRL Madrigal data base (http://madrigal.physics.colostate.edu/htdocs/). The Rayleigh lidar data from this study are available at: https://digitalcommons.usu.edu/all_datasets/29/.

References

Acott, P. E., She, C. Y., Krueger, D. A., Yan, Z., Yuan, T., Yue, J., & Harrell, S. (2011). Observed nocturnal gravity wave variances and zonal momentum flux in midlatitude mesopause region over Fort Collins, Colorado. *Journal of Atmospheric and Solar-Terrestrial Physics*, *73*(4), 449–456. https://doi.org/10.1016/j.jastp.2010.10.016

Argall, P. S. (2007). Upper altitude limit for Rayleigh lidar. *Annales Geophysicae*, *25*(1), 19–25. https://doi.org/10.5194/angeo-25-19-2007

Argall, P. S., & Sica, R. J. (2007). A comparison of Rayleigh and sodium lidar temperature climatologies. *Annales Geophysicae*, *25*(1), 27–35. https://doi.org/10.5194/angeo-25-27-2007

Argall, P. S., Vassiliev, O. N., Sica, R. J., & Mwangi, M. M. (2000). Lidar measurements taken with a large-aperture liquid mirror. 2. Sodium resonance-fluorescence system. *Applied Optics*, *39*(15), 2393–2400. https://doi.org/10.1364/AO.39.002393

Beig, G. P. K., Lowe, R. P., Roble, R. G., Mlynczak, M. G., Scheer, J., et al. (2003). Review of mesospheric temperature trends. *Reviews of Geophysics*, *41*(4), 1015. https://doi.org/10.1029/2002RG000121

Beissner, K. C. (1997). Studies of mid-latitude mesospheric temperature variability and its relationship to gravity waves, tides, and planetary waves. PhD Dissertation, 186 pp., *Utah State University*, Logan, UT. http://digitalcommons.usu.edu/etd/4687

Chapman, S. (1930). On ozone and atomic oxygen in the upper atmosphere. *Philosophical Magazine*, *10*(64), 369–383. https://doi.org/10.1080/14786443009461588

Chen, H., White, M. A., Krueger, D. A., & She, C. Y. (1996). Daytime mesopause temperature measurements with a sodium-vapor dispersive Faraday filter in a lidar receiver. *Optics Letters*, *21*(15), 1093–1095. https://doi.org/10.1364/OL.21.001093

Fleming, E. L., Chandra, S., Barnett, J. J., & Corney, M. (1990). COSPAR international reference atmosphere, chapter 2: Zonal mean temperature, pressure, zonal wind and geopotential height as functions of latitude. *Advances in Space Research*, *10*(12), 11–59. https://doi.org/10.1016/0273-1177(90)90386-E

Fricke, K. H., & von Zahn, U. (1985). Mesopause temperatures derived from probing the hyperfine structure of the D2 resonance line of sodium by lidar. *Journal of Atmospheric and Solar-Terrestrial Physics*, *47*(5), 499–512. https://doi.org/10.1016/0021-9169(85)90116-3

Funatsu, B. M., Claud, C., Keckhut, P., Steinbrecht, W., & Hauchecorne, A. (2011). Investigations of stratospheric temperature regional variability with lidar and advanced microwave sounding unit, 2011. *Journal of Geophysical Research*, *116*(D8), D08106. https://doi.org/10.1029/2010JD014974

Gao, Q., Chu, X., Xue, X., Dou, X., Chen, T., & Chen, J. (2015). Lidar observations of thermospheric Na layers up to 170 km with a descending tidal phase at Lijiang (26.7°N, 100.0°E) China. *Journal of Geophysical Research: Space Physics*, *120*, 9213–9220. https://doi.org/10.1002/2015JA021808

Gardner, C. S. (1989). Sodium resonance fluorescence lidar applications in atmospheric science and astronomy. *Proceedings of the IEEE*, *77*(3), 408–418. https://doi.org/10.1109/5.24127

Hauchecorne, A., & Chanin, M. -L. (1980). Density and temperature profiles obtained by lidar between 35 and 70 km. *Geophysical Research Letters*, *7*(8), 565–568. https://doi.org/10.1029/GL007i008p00565

Hauchecorne, A., Chanin, M.-L., & Keckhut, P. (1991). Climatology and trends of the middle atmospheric temperature (33–87 km) as seen by Rayleigh lidar over the south of France. *Journal of Geophysical Research*, *96*(D8), 15,297–15,309. https://doi.org/10.1029/91JD01213

Herron, J. P. (2004). Mesospheric temperature climatology above Utah State University. MS. thesis, 155 pp, *Utah State University*, Logan, UT. https://digitalcommons.usu.edu/etd/6877/

Herron, J. P. (2007). Rayleigh-scatter lidar observations at USU's Atmospheric Lidar Observatory (Logan, UT) — Temperature climatology, temperature comparisons with MSIS, and noctilucent clouds. PhD Dissertation, 156 pp., *Utah State University*, Logan, UT. https://digitalcommons.usu.edu/etd/4686

Herron, J. P., Wickwar, V. B., Espy, P. J., & Meriwether, J. W. (2007). Observation of a noctilucent cloud above Logan, Utah (41.7°N, 111.8°W) in 1995. *Journal of Geophysical Research*, *112*(D19), D19203. https://doi.org/10.1029/2006JD007158

Kent, G. S., & Wright, R. W. (1970). A review of laser radar measurements of atmospheric properties. *Journal of Atmospheric and Solar-Terrestrial Physics*, *32*(5), 917–943. https://doi.org/10.1016/0021-9169(70)90036-X

Krueger, D. A., She, C. Y., & Yuan, T. (2015). Retrieving mesopause temperature and line-of-sight wind from full-diurnal-cycle Na lidar observations. *Applied Optics*, *54*(32), 9469–9489. https://doi.org/10.1364/AO.54.009469

Leblanc, T., & McDermid, I. S. (1998). Evaluation and optimization of lidar temperature analysis algorithms using simulated data. *Journal of Geophysical Research*, *103*(D6), 6177–6187. https://doi.org/10.1029/97JD03494

Leblanc, T., McDermid, I. S., Keckhut, P., Hauchecorne, A., She, C. Y., & Krueger, D. A. (1998). Temperature climatology of the middle atmosphere from long-term lidar measurements at middle and low latitudes. *Journal of Geophysical Research*, *103*(D14), 17,191–17,204. https://doi.org/10.1029/98JD01347

Liu, A. Z., Guo, Y., Vargas, F., & Swenson, G. R. (2016). First measurement of horizontal wind and temperature in the lower thermosphere (105–140 km) with a Na lidar at Andes Lidar Observatory. *Geophysical Research Letters*, *43*(6), 2374–2380. https://doi.org/10.1002/2016GL068461

McCullough, E. M. (2015). A new technique for interpreting depolarization measurements using the CRL atmospheric lidar in the Canadian High Arctic. PhD dissertation, 316 pp., *University of Western Ontario,* London, Ontario, Canada. https://ir.lib.uwo.ca/etd/3418

Measures, R. M. (1992). *Laser remote sensing fundamentals and applications* (p. 510). Malabar, FL: Krieger Publishing Company.

Mwangi, M. M., Sica, R. J., & Argall, P. S. (2001). Retrieval of molecular nitrogen and molecular oxygen densities in the upper mesosphere and lower thermosphere using ground-based lidar measurements. *Journal of Geophysical Research*, *106*(D10), 10,313–10,323. https://doi.org/10.1029/2000JD900669

Picone, J. M., Hedin, A. E., Drob, D. P. & Aiken, A. C. (2002). NRLMSISE-00 empirical model of the atmosphere: Statistical comparisons and scientific issues. *Journal of Geophysical Research 107*(A12), 1468. https://doi.org/10.1029/2002JA009430

She, C. Y., Chen, H., & Krueger, D. A. (2015). Optical processes for middle atmospheric Doppler lidars: Cabannes scattering and laser-induced resonance fluorescence. *Journal of the Optical Society of America B*, *32*(8), 1575–1592. https://doi.org/10.1364/JOSAB.32.001575

She, C. Y., Chen, S., Hu, Z., Sherman, J., Vance, J. D., Vasoli, V., et al. (2000). Eight-year climatology of nocturnal temperature and sodium density in the mesopause region (80 to 105 km) over Fort Collins, Co (41°N, 105°W). *Geophysical Research Letters*, *27*(20), 3289–3292. https://doi.org/10.1029/2000GL003825

She, C.-Y., Krueger, D. A., & Yuan, T. (2015). Long-term midlatitude mesopause region temperature trend deduced from quarter century (1990–2014) Na lidar observations. *Annales Geophysicae*, *33*(3), 363–369. https://doi.org/10.5194/angeo-33-363-2015

She, C. Y., Yu, J. R., Latifi, H., & Bills, R. E. (1992). High-spectral-resolution fluorescence light detection and ranging for mesospheric sodium temperature measurements. *Applied Optics*, *31*(12), 2095–2106. https://doi.org/10.1364/AO.31.002095

Sox, L. (2016). Rayleigh-scatter lidar measurements of the mesosphere and thermosphere and their connections to sudden stratospheric warmings. PhD dissertation, 212 pp., *Utah State University*, Logan, UT. https://digitalcommons.usu.edu/etd/5227

States, R. J., & Gardner, C. S. (2000). Temperature structure of the mesopause region (80–105 km) at 40°N latitude, 1, Seasonal variations. *Journal of the Atmospheric Sciences*, *57*(1), 66–77. https://doi.org/10.1175/1520-0469(2000)057<0066:TSOTMR>2.0.CO;2.

Wickwar, V. B., Sox, L., Emerick, M. T., Herron, J. P., & Barton D. L. (2016). Early observations with the extremely sensitive Rayleigh lidar at Utah State University. EPJ Web of Conferences, 119, 13007. doi:https://doi.org/10.1051/epjconf/201611913007

Wulf, O. R., & Deming, L. S. (1938). On the production of the ionospheric regions E and F and the lower-altitude ionization causing radio fade-outs. *Terrestrial Magnetism and Atmospheric Electricity*, *43*(3), 283–298. https://doi.org/10.1029/TE043i003p00283

Wynn, T. A. (2010). Statistical analysis of the USU lidar data set with reference to mesospheric solar response and cooling rate calculation, with analysis of statistical issues affecting the regression coefficients. PhD dissertation, 280 pp., *Utah State University*, Logan, UT. https://digitalcommons.usu.edu/etd/797

Yuan, T., Pautet, P.-D., Zhao, Y., Cai, X., Criddle, N. R., Taylor, M. J., & Pendleton, W. R. Jr. (2014). Coordinated investigation of midlatitude upper mesospheric temperature inversion layers and the associated gravity wave forcing by Na lidar and Advanced Mesospheric Temperature Mapper in Logan, Utah. *Journal of Geophysical Research: Atmospheres*, *119*(7), 3756–3769. https://doi.org/10.1002/2013JD020586

Yuan, T., She, C.-Y., Kawahara, T. D., & Krueger, D. A. (2012). Seasonal variations of midlatitude mesospheric Na layer and its tidal period perturbations based on full diurnal cycle Na lidar observations of 2002–2008. *Journal of Geophysical Research*, *117*(D11), D11304. https://doi.org/10.1029/2011JD017031

Yuan, T., She, C.-Y., Krueger, D. A., Sassi, F., Garcia, R., Roble, R. G., et al. (2008). Climatology of mesopause region temperature, zonal wind, and meridional wind over Fort Collins, Colorado (41°N, 105°W), and comparison with model simulations. *Journal of Geophysical Research*, *113*(D3), D03105. https://doi.org/10.1029/2007JD008697

Yuan, T., Yue, J., She, C. Y., Sherman, J. P., White, M. A., Harrell, S. D., et al. (2009). Wind-bias correction method for narrowband sodium Doppler lidars using iodine absorption spectroscopy. *Applied Optics*, *48*(20), 3988–3993. https://doi.org/10.1364/AO.48.003988